

Barometric tides from ECMWF operational analyses

R. D. Ray¹ and R. M. Ponte²

¹NASA Goddard Space Flight Center, Greenbelt, Maryland, USA

²Atmospheric and Environmental Research, Inc., Lexington, Massachusetts, USA

Abstract

The solar diurnal and semidiurnal tidal oscillations in surface pressure are extracted from the the operational analysis product of the European Centre for Medium Range Weather Forecasting (ECMWF). For the semidiurnal tide this involves a special temporal interpolation, following Van den Dool and colleagues. The resulting tides are compared with a “ground truth” tide dataset, a compilation of well-determined tide estimates deduced from long time series of station barometer measurements. These comparisons show that the ECMWF tides are significantly more accurate than the tides deduced from two other widely available reanalysis products. Spectral analysis of ECMWF pressure series shows that the tides consist of sharp central peaks with modulating sidelines at integer multiples of 1 cycle/year, superimposed on a broad cusp of stochastic energy. The integrated energy in the cusp dominates that of the sidelines. This complicates development of a simple model that can characterize the full temporal variability of the tides.

Key words. 3384 Waves and tides

1 Introduction

The spectrum of atmospheric surface pressure exhibits strong peaks at diurnal and semidiurnal periods, a well-known manifestation of the solar atmospheric tides. These global atmospheric oscillations, forced primarily by water-vapor and ozone radiational absorption, constitute a major part of the total surface pressure variance in the tropics and contribute importantly to the local daily cycle elsewhere. The tides have long been studied both in their own right (Chapman and Lindzen, 1970) and for what they potentially reveal about the atmosphere (e.g., Wilkes, 1949; Cooper, 1982; Hamilton, 1983; Braswell and Lindzen, 1998). Our work is partly motivated by modern oceanographic and geodetic applications: tidal pressure waves load the ocean and land, and the resulting deformations must be precisely modeled when analyzing, for example, sea level (Ponte and Gaspar, 1999) or gravity (Wahr et al., 1998). For these and other applications, globally well-resolved barometric tides $S_1(p)$ and $S_2(p)$ are required.

Global $S_1(p)$ and $S_2(p)$ fields have traditionally been constructed by empirical means (e.g., Haurwitz and Cowley, 1973; Dai and Wang, 1999; Ray, 2001). Tidal harmonic analyses of hourly barometric measurements, taken at a large number of globally distributed stations can be spatially interpolated (optimally or otherwise) to yield globally gridded fields. More recently, estimates based on general circulation models (Zwiers and Hamilton, 1986; Madden et al., 1998) and on analyses produced by weather centers (Hsu and Hoskins, 1989; Van den Dool et al., 1997; Ray, 2001) have also been examined. The latter products are of special interest because they are based on “optimal” estimates of the state of the atmosphere arrived at through advanced modeling and data assimilation techniques. Gridded analysis fields have a typical 6-hour sampling interval, however, which leads to S_2 solutions that are standing, rather than westward propagating, and with much underestimated amplitudes near longitudes where sampling times happen to coincide with times of the S_2 nodes. Temporal interpolation methods can be used to recover the fully propagating S_2 tide (Van den Dool et al., 1997), but their general usefulness remains to be tested.

Comparisons of global barometric tides derived from the available gridded analyses with the meteorological station data provide a useful test of the analyzed fields and also the interpolation methods (Van den Dool et al., 1997). Ray (2001) examined $S_2(p)$ in the reanalyses of the National Centers for Environmental Prediction–National Center for Atmospheric Research (NCEP-NCAR), as interpolated by Van den Dool et al. (1997), and the NASA Goddard Earth Observing System (GEOS-1), for which 3-hour fields were available and no interpolation was required. Comparisons with data revealed significant inadequacies in the representation of $S_2(p)$ in both reanalyses (Ray, 2001). Similar detailed comparisons for $S_1(p)$ are missing, but significant discrepancies between theoretical and observed estimates have been noted (Braswell and Lindzen, 1998; Ray, 1998).

In this paper, we examine $S_1(p)$ and $S_2(p)$ solutions based on the operational analyses of the European Centre for Medium-Range Weather Forecasts (ECMWF) (Hsu and Hoskins, 1989). We find that these solutions are far more accurate than those from the two reanalysis fields considered by Ray (2001).

In what follows, we first describe the ECMWF fields and the methodology used to create climatological daily cycles of surface pressure (section 2), and then discuss in detail respective $S_2(p)$ and $S_1(p)$ solutions

in comparison with those from other analyses (Ray, 2001) and the barometer data (sections 3 and 4). An important aspect of the atmospheric tides is their variability (Chapman and Lindzen, 1970; Lindzen, 1990), and both spectral analysis and monthly climatologies are used to assess these effects in the ECMWF fields (section 5).

2 Daily cycle in ECMWF surface pressure fields

2.1 Six-hourly climatologies

Surface pressure analyses from ECMWF were obtained from the archives at NCAR for the period 1986–1998. Prior to 1986 ECMWF analyses were provided on coarser grids, and at the start of our study 1998 was the last complete year in the NCAR archives. For the 13-year period considered, surface pressure fields were available four times daily (0000, 0600, 1200, and 1800 UT) on a regular 1.125° grid in longitude and gaussian grid in latitude with 160 points. Values were interpolated in latitude to a regular 1.125° grid to facilitate analyses. For the purposes of studying seasonal modulations of the barometric tides, we calculated monthly climatologies of the daily cycle in p_a . For each month all the analyses at each given time of day (totaling the number of days in respective month times 13 years) were averaged to obtain four mean fields at 0000, 0600, 1200, and 1800 UT. Results in the paper are based on these monthly climatologies with the daily time mean at each grid point removed.

Figure 1 shows the 13-year averaged daily cycle in p_a obtained by averaging the 12 monthly climatologies. A clear zonal wavenumber-two pattern, approximately alternating in sign every 6 hours, underlines the dominant presence of the S_2 tide, but its westward propagation cannot be discerned from the 6-hourly maps. The differences in patterns separated by 12 hours also hint at the presence of variability associated with the S_1 tide. Amplitudes are largest in the tropics and decay to small values at high latitudes. Spatial variations are smooth over the oceans but shorter scale structures appear over land and particularly so over high orography. In general, the overall characteristics of the ECMWF daily cycle in p_a are consistent with past theoretical and observational studies of the air tides (Lindzen, 1990; Dai and Wang, 1999). ECMWF results are also broadly similar to the climatologies based on the NCEP/NCAR reanalysis (Van den Dool et al., 1997), although ECMWF peak amplitudes are consistently smaller by ~ 0.5 mb in the tropics.

As a preliminary assessment of seasonal effects, Figures 2 and 3 show p_a maps for March and June climatologies, respectively. At low latitudes amplitudes are larger in March than in June by ~ 0.5 mb, indicating a substantial semiannual modulation of the wavenumber-two pattern associated with S_2 . Stronger amplitudes in March coincide with the maximum solar insolation (and thus strongest forcing) over tropical regions. Peak amplitudes do not particularly follow the shift in maximum solar insolation from the equator in March to the tropic of Cancer in June, which is not unexpected since the atmosphere's response to radiational forcing is dominated by equatorially symmetric modes (Lindzen, 1990). Comparisons between June and December climatologies (not shown) nevertheless indicate that the response over land and land-ocean contrasts are enhanced in the summer hemisphere. Substantial annual modulation of S_1 signals over

land are, therefore, expected. More detailed discussion of seasonal effects is given below when examining S_1 and S_2 solutions.

2.2 Time interpolated climatologies

As previously discussed, the 6-hourly fields in Figure 1 cannot represent the propagating S_2 signals. For proper resolution of the S_2 tide, we followed essentially the interpolating method developed by Van den Dool et al. (1997), which implicitly assumes that the barometric tide propagates westward with the Sun at approximately $15^\circ/\text{hour}$. Merely shifting one pattern by 90° westward in Figure 1 does not yield the observed pattern 6 hours later, however, partly because of the presence of nonmigrating tidal signals. Non-migrating components associated with land features and having relatively short spatial scales have been noted (Figure 1). To minimize the effects of such signals on the interpolation, at each latitude filtering was applied to the climatological fields to retain only the zonal mean plus the first 10 zonal wavenumbers, as in Van den Dool et al. (1997). The S_2 solutions described below were not overly sensitive to the filter wavenumber cutoff and results with more smoothing did not lead to any measurable improvements.

Given the longitudinal grid spacing of 1.125° , we chose to create an interpolated series at 45 minute intervals, which gave an integral number of grid points (10) for the distance traveled by the tides between samples. The interpolation procedure was as in Van den Dool et al. (1997) with one difference: the filtered p_a patterns were assumed to propagate at the nominal rate of $15^\circ/\text{hour}$ without any differential phase adjustments for the various zonal wavenumbers. Van den Dool et al. noted that the phase propagation of each wavenumber can deviate from the expected values and tried to allow for such dispersion effects. The determination of the phase propagation was, however, ambiguous. For simplicity, we have ignored these effects in our procedure.

To create interpolated values at any time $t_a + \delta t$ in hours, where t_a is a time for which an analysis is available, the following procedure was applied: (1) the climatological pattern at t_a was propagated westward by a distance $15^\circ \times \delta t$ to yield W ; (2) the next available climatological pattern at $t_a + 6$ was propagated eastward by a distance of $15^\circ \times (6 - \delta t)$ to yield E ; (3) the two resulting fields were averaged as $[(6 - \delta t) \times W + \delta t \times E]/6$. Interpolated solutions are thus exactly equal to the observed (filtered) climatologies at 0000, 0600, 1200, and 1800 and correspond to a weighted average of two closest patterns at other times, with propagation effects accounted for by the shifting in (1) and (2). Figure 4 shows, as an example, the resulting 13-year average daily cycle in p_a at 1.5 hour intervals. The p_a patterns exhibit little contamination by short scale land effects and progress smoothly westward in time as intended.

3 Annual mean S_2 tide

Global charts of the amplitude and phase of the S_2 tide can be readily extracted from the interpolated fields of Figure 4 by least squares fit to a simple sinusoid at every geographic location:

$$S_2(p) = A_2 \cos(2T - \varphi_2) \quad (1)$$

The results are shown in Figure 5. With T taken as Universal Time (in appropriate units) the phase φ is a “Greenwich phase lag” as traditionally employed in ocean-tide studies. By tracing out successive contours of φ the high-pressure peak of $S_2(p)$ can be easily followed in time. Figure 5 shows it marching westward, slightly leading the sun by roughly 60° , or about 2 hours, a well-known feature of S_2 .

Similar figures have been computed from other reanalysis surface pressure fields (e.g., Dai and Wang, 1999; Ray, 2001) and from simulations (e.g., Zwiers and Hamilton, 1986). The annual mean S_2 tide derived from the NASA Goddard Earth Observing System (GEOS-1) reanalysis (Schubert et al., 1993) and from the NCEP/NCAR reanalysis (Kalnay et al., 1996), temporally interpolated by Van den Dool et al. (1997), were extensively compared by Ray (2001). Comparison of Figure 5 with corresponding NCEP/NCAR and GEOS-1 charts (Figures 2 and 3 of Ray, 2001) shows gross similarities but also shows some immediate differences. The ECMWF tidal amplitudes are smaller in the tropical latitudes than NCEP and more zonally symmetric than GEOS-1. The NCEP amplitudes are thought to be too large (Van den Dool et al., 1997).

More quantitative comparisons and tests of these S_2 fields can be obtained by employing the set of “ground truth” S_2 estimates of Ray (2001). These are tide estimates based on analyses of long time series of barometric pressure measurements from 428 widely distributed meteorological stations. This set of station estimates is a merger of three previous compilations by Haurwitz (1956), Hamilton (1980), and Ray (1998). Considerable care was taken in deriving each of the tidal estimates, and they likely represent the best “ground truth” knowledge we have of the S_2 tide. Table 1 summarizes the root-mean-square (rms) and median absolute differences (MAD) between the 428 stations and each of the three gridded products we have at our disposal. In all cases our temporally interpolated ECMWF fields appear to yield the more accurate estimates of S_2 .

Figure 6 shows the amplitude and phase differences between the ECMWF tide and each of the 428 station estimates, plotted as a function of latitude. Amplitude differences are noticeably larger and more scattered in tropical latitudes where the tide itself is maximum. At first glance, and consistent with Table 1, this scatter is less pronounced than in similar diagrams for NCEP and GEOS-1 (Ray, 2001, Figures 5 and 6). Also noticeable in Figure 6 (top) is a consistent phase discrepancy between ECMWF and the test stations. Except for a small band near the equator, all latitudes between 60°N and 60°S suggest that the ECMWF phases φ are too large. (Larger phase scatter in high latitudes is of no significance because of the very small amplitudes.) The mean phase discrepancy in Figure 6 is 9.7° ; the median is 10.4° . A phase error of 10° implies that the ECMWF S_2 tide is generally too late by 20 minutes. Similar phase discrepancies were noticed in the other two reanalysis tides (Ray, 2001), with NCEP too late by roughly 30 minutes and GEOS-1 too early by roughly 60 minutes (depending on how the time-tag in the GEOS product is interpreted). We are not in a position to offer credible explanations for the cause of such time discrepancies, except to say that they appear to be fairly robust (as in Figure 6) and that the errors cannot be in the station data. The statistics of Table 1 show the model-station comparisons both before and after the model phases have been corrected, and the statistics for the corrected phases are lower, as expected. (Both NCEP and GEOS-1 statistics reflect phases already corrected for their deduced systematic errors, as discussed more fully in Ray [2001].)

A possibly legitimate criticism of Figure 5 is that the map may be too zonally symmetric, an artificial byproduct of the wavenumber filtering employed by us and by Van den Dool et al. (1997). In fact, examination of the Figure-1 mean pressures suggests that S_2 may well embody significant non-migrating components—note, for example, the outline of Australia evident in several of the diagrams of Figure 1. Such land-fixed features are evident in the GEOS-1 semidiurnal tide, which was deduced directly from the 3-h pressure data without wavenumber filtering (Dai and Wang, 1999; Ray, 2001), and which may thus be more realistic in this regard than our Figure 5. Yet the few features that can be tested by the ground-truth stations suggest that the non-migrating GEOS-1 features must be treated with caution. For example, while the amplitude contours in Figure 5 are almost perfectly east-west across the North Atlantic Ocean, the GEOS-1 amplitudes collapse to a minimum at mid-ocean (Dai and Wang, 1999, Figure 16); the ground-truth stations, however, suggest no such collapse (Ray, 2001).

Given the 6-h ECMWF sampling, it is impossible to recover unambiguously any real non-migrating component of S_2 . We can, however, restore the non-migrating in-phase component $A_2 \cos \varphi_2$ by fitting a sinusoidal wave to the difference between our model Eq. (1) and the data of Figure 1. The modified S_2 amplitude and phase charts are shown in Figure 7, and the relevant ground-truth statistics are listed in Table 1 under the label “ECMWF(2).” According to Table 1 the land regions of the new solution, and especially the high-altitude regions, are more accurate, but the oceanic regions are degraded, and the overall accuracy is about the same.

4 Annual Mean S_1 Tide

Similar charts may be derived for the diurnal $S_1(p)$ tide. In this case, however, it is important to minimize any wavenumber filtering because it is well known (Haurwitz and Cowley, 1973) that S_1 is dominated by large non-migrating components with complicated spatial distributions. The S_1 tide is evidently susceptible to significant diurnal boundary-layer effects over land masses and land-ocean boundaries. We therefore avoid altogether using our temporally interpolated fields to deduce S_1 and return to the original 6-hourly fields of Figure 1, which are sufficient to determine a diurnal wave.

At each geographical location we fit to the four mean pressure fields (i.e., unfiltered fields at 0000, 0600, 1200, and 1800 UT as given in Figure 1) a sinusoid of form

$$S_1(p) = A_1 \cos(T - \varphi_1). \quad (2)$$

The resulting amplitudes A_1 and phase lags φ_1 are shown in Figure 8. The spatial complexity of these fields is highly pronounced relative to the simple semidiurnal wave of Figure 5. Large non-migrating amplitudes, fixed to certain land features, are clearly apparent. The main migrating component is most apparent over the tropical oceans where the phases again show an approximately constant westward march, now lagging the sun by roughly 250° , or 17 hours (or, equivalently, leading the sun by roughly 7 hours). From Figure 8 this migrating (zonal wavenumber-one) component is no more than perhaps half the size of the semidiurnal

wave, while the non-migrating components in some regions (e.g., South America) exceed all semidiurnal amplitudes.

It would be highly desirable to compare the S_1 tide of Figure 8 and other reanalysis tides against a “ground truth” dataset similar to that used above for S_2 . Unfortunately, we know of no similar compilation that is reliable. Our efforts to locate Bernard Haurwitz’s old compilation have so far proven futile. As a makeshift, but limited, test dataset we adopt a set of 25 S_1 station estimates from small oceanic islands (Ray, 1998). This set of oceanic stations is, of course, completely inadequate for testing tidal fields over the continents where the S_1 signal is largest, but it is nonetheless valuable in two ways: as a test of the predominantly migrating S_1 component, which appears to be best isolated in oceanic stations, and as a reliability test of the oceanic diurnal pressure forcing for those investigators interested in sea level. Comparisons against this 25-station set of S_1 estimates are given in Table 2. The required NCEP and GEOS-1 S_1 fields were deduced in similar fashion to the S_2 fields described above, with the NCEP results based on non-interpolated 6-hour grids.

Our 25-station test set is too limited to allow a reliable independent estimate of any systematic phase error, as seen above for S_2 . If the error is caused by a simple time-tag problem (perhaps related to the times that data are ingested into the analysis), then the observed S_2 error of 10° implies a 5° error in S_1 . Applying a 5° shift to the S_1 phases does reduce the rms difference with the 25 station estimates (although the median absolute difference is unchanged). This rms reduction is thus consistent with a 20-minute error in the ECMWF pressures.

Table 2 also lists the rms and median absolute differences between the 25 stations and the NCEP and GEOS-1 diurnal tides. As the statistics make clear, the ECMWF S_1 estimates are the most reliable of the three products. We emphasize that this statement applies exclusively to the oceanic regions, since none of the 25 stations is from continental regions.

5 Variability of ECMWF Tides

Significant variability in atmospheric tides is a well known fact (e.g., Chapman and Lindzen, 1970; Haurwitz and Cowley, 1973). In this section we examine the nature of this variability as implied by the ECMWF series.

5.1 Monthly analyses

A standard approach to studying variability in atmospheric tides is to concentrate on seasonal variations, either in terms of monthly means or in terms of the so-called Lloyd seasons (winter, summer, equinoctial); see, for example, Chapman and Lindzen (1970). It is straightforward to form monthly estimates of $S_1(p)$ and $S_2(p)$ from the monthly climatologies discussed in Section 2. Figures 9 and 10 show the resulting amplitudes of both tides.

The annual and semiannual modulations in S_2 are very clear in Figure 9. In low latitudes the smallest

amplitudes occur during June and July, but the largest occur during the two equinoctial seasons of March-April and September-October. This is, of course, consistent with some of the features discussed in the context of Figures 2 and 3 above. The same pattern of reduced tropical amplitudes in June and July and strongest amplitudes during equinoctial months appears to hold also for S_1 , although this is less obvious because of the exceedingly complex spatial patterns.

Figures 11 and 12 summarize the tropical responses by depicting the in-phase and out-of-phase tidal components averaged over all tropical regions of the globe. (Such diagrams are essentially equivalent to Chapman's "harmonic dials".) To allow proper zonal averaging for these figures, we have converted all phase lags to correspond to mean local solar time: $\kappa_n = \varphi_n + n\lambda$ where λ is east longitude and n is 1 for diurnal and 2 for semidiurnal. (Phases have also been adjusted for the systematic error noted in Figure 6.) Figure 11 shows an unsymmetrical three-leaf clover pattern for S_2 , which is consistent with dominant annual and semi-annual modulations. Again the smallest amplitudes are clearly in the northern summer months, while northern winter amplitudes are near the annual mean. Figure 12 separates the tropics into oceanic and land regions because of their dissimilar responses, which is primarily in the large quadrature $A_1 \sin \kappa_1$ component (i.e., the component corresponding to 6:00 local time). Smallest amplitudes are again in June and July, but otherwise the oceanic regions are dominated by the annual modulation whereas the land regions have a strong semi-annual modulation with relatively weak amplitudes in January and December.

In passing we might mention that Figures 11 and 12 show both the strengths and the weaknesses of the Lloyd system of averaging. While the "J season" of May–August gives fairly consistent estimates for all three diagrams, the "D season" of November–February includes a very wide range of phases, if not of amplitudes. Averaging such data into one "season" is of doubtful utility.

5.2 Spectral analysis

A complementary approach to understanding variability in tides is afforded by spectral analysis of the original surface pressure time series. This approach highlights some of the limitations of using simple monthly means. Wunsch and Stammer (1997) computed the frequency-wavenumber spectrum of the ECMWF surface pressures, and we here follow up on their work by studying in more detail the spectral structure near the tidal peaks. Wunsch and Stammer display the two-dimensional spectrum, which we need not reproduce here. The two-dimensional spectrum may be summed over all wavenumbers to yield a simple one-dimensional frequency spectrum representative of the global pressure field (for details, although in an oceanographic context, see Wunsch and Stammer, 1995).

Figure 13 shows the frequency spectrum estimated from four full years of six-hourly ECMWF surface pressures (years 1996–1999). Although no spectral smoothing has been performed, the spectrum is still relatively smooth because summation over all wavenumbers significantly reduces random noise, thus allowing the delineation of some very subtle spectral features. There are clear peaks at the annual (0.0027 cpd) and semi-annual (0.0055 cpd) frequencies and at the S_1 and S_2 tidal frequencies, the latter occurring at the ECMWF Nyquist frequency. (Compare the somewhat similar Figure 9 of Ponte, 1993.) There are

also some curious small peaks between the two tidal frequencies; close examination shows them occurring at frequencies 1.314, 1.628, 1.685, and 1.932 cpd. The latter is the expected lunar tide M_2 , but the others are unexpected and correspond to no tidal or modal period that we are aware of (e.g., Hamilton and Garcia (1986) find several modal peaks in the Batavia pressure spectrum but none corresponds to Figure-13 frequencies). The first two peaks are apparent harmonics of an S_1 modulation, since they are equidistant from 1.0 cpd. Our conjecture is that these peaks are likely spurious, related to some feature of the ECMWF processing.

Figure 14 is a “zoom” view of Figure 13 near 1 and 2 cpd. One sees the detailed fine structure around the tidal peaks (the fundamental spectral resolution is here 0.25 cpy). There is a clear broad cusp of enhanced energy surrounding both tidal peaks. This cusp spans a frequency range of roughly ± 0.01 cpd either side of the main spectral line. In addition to the cusp, and most prominent in S_1 , there are modulations of the main peaks at integral multiples of once per year. For S_1 the annual modulations are relative strong, each representing about a tenth the energy of the main line. This is consistent particularly with the oceanic regions of Figure 12. For S_2 only the semiannual modulation is apparent; if an annual modulation peak exists, it is buried within the cusp. Presumably the S_2 tide has similar structure above the Nyquist frequency which is folded back into frequencies below 2 cpd.

Table 3 summarizes the integrated spectral densities over the appropriate frequency ranges that surround the tidal peaks of Figure 14. In both diurnal and semidiurnal cases the cusps represent comparable energy, about $(0.2 \text{ mb})^2$, while the modulating sidelines represent significantly smaller amounts, although more in the diurnal band than semidiurnal. In relation to the main peak, variability is more important for the diurnal tide. (Note that the values for the main peaks in Table 3 are reasonably consistent with the global S_2 and S_1 amplitude fields shown in Figures 5 and 8, respectively: for these fields the rms over a complete tidal cycle is $570 \mu\text{b}$ for S_2 , corresponding to a variance of 3300 Pa^2 , and $315 \mu\text{b}$ for S_1 , corresponding to a variance of 1000 Pa^2 .)

From Figure 14 we conclude that the ECMWF tides display modulations at once and twice per year (and even tiny further peaks at 3, 4, and 5 times per year), but that these modulations are dominated by a complex cusp of incoherent, essentially stochastic, energy that complicates development of simple models. For example, the monthly means of Figures 9 and 10 could be adequately represented by an annual modulation and a few higher harmonics, but such a model would fail to capture the majority of the tidal variability that resides within the cusps.

6 Summary Remarks

Thirteen years of operational ECMWF fields were used to construct monthly climatologies of the daily cycle in surface pressure for the study of the $S_2(p)$ and $S_1(p)$ tides. Comparisons with station pressure data and products from other weather centers showed that the $S_2(p)$ and $S_1(p)$ tides are well represented in the ECMWF analysis. The available 6-hourly fields sample the S_2 tide at its Nyquist frequency, but our findings

indicate that simple time interpolation schemes, as proposed by Van den Dool et al. (1997) and used here, can work well in extracting the propagating S_2 tide. The ECMWF tides were found to have a phase bias of ~ 20 minutes relative to the observations. Such a shift in time can be easily corrected a posteriori, but the reasons behind it remain unclear.

Analyses of the monthly climatologies and four years (1996–1999) of 6-hourly fields revealed a complex seasonal modulation of the tides superimposed on an apparently more important cusp of variability at interannual and other shorter periods. The 4-year series analyzed in Figure 14 does not permit, however, a full evaluation of the interannual and longer period variability of the tides. Furthermore, a strong El Niño occurred in 1997–98 and may have affected the estimated tidal variability at interannual periods in Figure 14. The study of longer records would be needed to better quantify the variability of the S_1 and S_2 tides, and in particular, the size of the annual and semiannual modulations relative to variability at longer periods.

Acknowledgements. P. Nelson (AER) helped with initial processing of pressure fields. Support for work at AER was provided by NASA Jason-1 Project under contract 1206432 with the Jet Propulsion Laboratory.

References

- Braswell, W. D., and Lindzen, R. S.: Anomalous short wave absorption and atmospheric tides, *Geophys. Res. Lett.*, 25, 1293–1296, 1998.
- Chapman, S. and Lindzen, R.: *Atmospheric Tides*, Gordon and Breach, New York, 1970.
- Chapman, S., and Westfold, K. C.: A comparison of the annual mean solar and lunar atmospheric tides in barometric pressure as regards their worldwide distribution of amplitude and phase, *J. Atmos. Terr. Phys.*, 8, 1–23, 1956.
- Cooper, N. S.: Inferring solar UV variability from the atmospheric tide, *Nature*, 296, 131–132, 1982.
- Dai, A., and Wang, J.: Diurnal and semidiurnal tides in global surface pressure data, *J. Atmos. Sci.*, 56, 3874–3891, 1999.
- Hamilton, K.: The geographical distribution of the solar semidiurnal surface pressure oscillation, *J. Geophys. Res.*, 85, 1945–1949, 1980.
- Hamilton, K.: Quasi-biennial and other long period variations in the solar semidiurnal barometric oscillation: observations, theory, and possible application to the problem of monitoring changes in global ozone, *J. Atmos. Sci.*, 40, 2432–2443, 1983.
- Hamilton, K. and Garcia, R. R.: Theory and observations of the short-period normal mode oscillations of the atmosphere, *J. Geophys. Res.*, 91, 11867–11875, 1986.
- Haurwitz, B.: The geographical distribution of the solar semidiurnal pressure oscillation. New York University, College of Engineering, *Meteorological Papers*, Vol. 2, No. 5, 36 pp, 1956.
- Haurwitz, B., and Cowley, A. D.: The diurnal and semidiurnal barometric oscillations, global distribution and annual variation, *Pure Appl. Geophys.*, 102, 193–222, 1973.
- Hsu, H.-H., and Hoskins, B. J.: Tidal fluctuations as seen in ECMWF data, *Q. J. R. Meteorol. Soc.*, 115, 247–264, 1989.
- Kalnay, E. et al.: The NCEP/NCAR 40 year reanalysis project, *Bull. Am. Met. Soc.*, 77, 437–471, 1996.
- Lindzen, R. S.: *Dynamics of Atmospheric Physics*, Cambridge Univ. Press, New York, 1990.
- Madden, R. A., Lejenäs, H., and Hack, J.: Semidiurnal variations in the budget of angular momentum in a general circulation model and in the real atmosphere, *J. Atmos. Sci.*, 55, 2561–2575, 1998.
- Ponte, R. M.: Variability in a homogeneous global ocean forced by barometric pressure, *Dyn. Atmos. Oceans*, 18, 209–234, 1993.
- Ponte, R. M., and Gaspar, P.: Regional analysis of the inverted barometer effect over the global ocean using TOPEX/POSEIDON data and model results, *J. Geophys. Res.*, 104, 15,587–15,601, 1999.
- Ray, R. D.: Diurnal oscillations in atmospheric pressure at twenty-five small oceanic islands, *Geophys. Res. Lett.*, 25, 3851–3854, 1998.
- Ray, R. D.: Comparisons of global analyses and station observations of the S_2 barometric tide, *J. Atmos. Solar-Terr. Phys.*, 63, 1085–1097, 2001.
- Schubert, S. D., R. B. Rood, and J. Pfandtner, An assimilated data set for earth science applications, *Bull. Am. Met. Soc.*, 74, 2331–2342, 1993.
- Van den Dool, H. M., Saha, S., Schemm, J., and Huang, J.: A temporal interpolation method to obtain hourly atmospheric surface pressure tides in Reanalysis 1979–1995, *J. Geophys. Res.*, 102, 22013–22024, 1997.
- Wahr, J., Molenaar, M., and Bryan, F.: Time variability of the Earth's gravity field: hydrological and oceanic effects and their possible detection using GRACE, *J. Geophys. Res.*, 103, 30205–30229, 1998.

- Wilkes, M. V.: *Oscillations of the Earth's Atmosphere*, Cambridge Univ. Press, 1949
- Wunsch, C., and Stammer, D.: The global frequency-wavenumber spectrum of oceanic variability estimated from Topex/Poseidon altimetric measurements, *J. Geophys. Res.*, 100, 24895–24910, 1995.
- Wunsch, C., and Stammer, D.: Atmospheric loading and the oceanic “inverted barometer” effect, *Rev. Geophys.*, 35, 79–107, 1997.
- Zwiers, F., and Hamilton, K.: Simulation of solar tides in the Canadian Climate Centre general circulation model, *J. Geophys. Res.*, 91, 11877–11896, 1986.

Tables

Table 1. S_2 rms differences (μb) with station estimates.

	all stations	above 1000 m	latitude $\leq 30^\circ$	ocean stations	MAD*
NCEP	151	245	296	208	82
GEOS	168	196	300	238	85
ECMWF†	124	177	243	211	69
ECMWF	112	159	230	134	52
ECMWF(2)	110	141	221	156	54

* Median Absolute Difference

† Before phase correction

Of 428 stations, 42 are above 1000 meters, 157 are low latitude, 46 are classified oceanic. Solution ECMWF(2) corresponds to Figure 7.

Table 2. S_1 differences (μb) with 25 ocean stations.

	RMS	MAD*
NCEP	112	81
GEOS	124	73
ECMWF†	74	51
ECMWF	66	51

* Median Absolute Difference

† Before phase correction

Table 3. Integrated energy in tidal bands, Pa^2

	S_1	S_2
Primary line	1070	3300
Secondary sideline(s)	120	30
Incoherent cusp	310	500

Figure Captions

Fig. 1. Climatological daily cycle of surface pressure (mbar) calculated from 13 years of ECMWF analyses at 0000, 0600, 1200, and 1800 UT. Negative values are shaded. Contour interval is 0.4 mb.

Fig. 2. As in Figure 1 but showing climatological daily cycle for March.

Fig. 3. As in Figure 1 but showing climatological daily cycle for June.

Fig. 4. Interpolated climatological daily cycle at 1.5 hour intervals. Time marches horizontally from the top left corner (0000 UT) to the bottom right corner (2230 UT).

Fig. 5. Amplitude (μb) and Greenwich phase lags (degrees) of the $S_2(p)$ tide, calculated as described in the text. The phase contour interval of 30° corresponds to 1 hour in time.

Fig. 6. Amplitude and phase differences between ECMWF-implied $S_2(p)$ tide and estimates based on 428 barometer stations. A small systematic error in the phases is readily apparent.

Fig. 7. Amplitude (μb) and Greenwich phase lags (degrees) of the $S_2(p)$ tide, as in Figure 5, except with the in-phase non-migrating component restored. This solution is denoted "ECMWF(2)" in Table 1.

Fig. 8. Amplitude and Greenwich phase lags of the $S_1(p)$ tide, as deduced from ECMWF surface pressures.

Fig. 9. Monthly mean amplitude of the $S_2(p)$ tide as deduced from ECMWF surface pressures.

Fig. 10. Monthly mean amplitude of the $S_1(p)$ tide as deduced from ECMWF surface pressures.

Fig. 11. Monthly estimates of the in-phase ($A_2 \cos \kappa_2$) and quadrature ($A_2 \sin \kappa_2$) components of the $S_2(p)$ tide, averaged over all tropical regions (latitudes $\leq 23^\circ$). Months are labeled 1–12.

Fig. 12. As in Figure 11 but for $S_1(p)$, and separated into tropical ocean and land regions.

Fig. 13. Spectrum of the globally integrated ECMWF p_a series, based on the four-year span 1996-1999.

Fig. 14. Detailed views of the spectrum of Figure 13 surrounding the diurnal and semidiurnal peaks. Frequency resolution is 0.25 cpy.

Figures

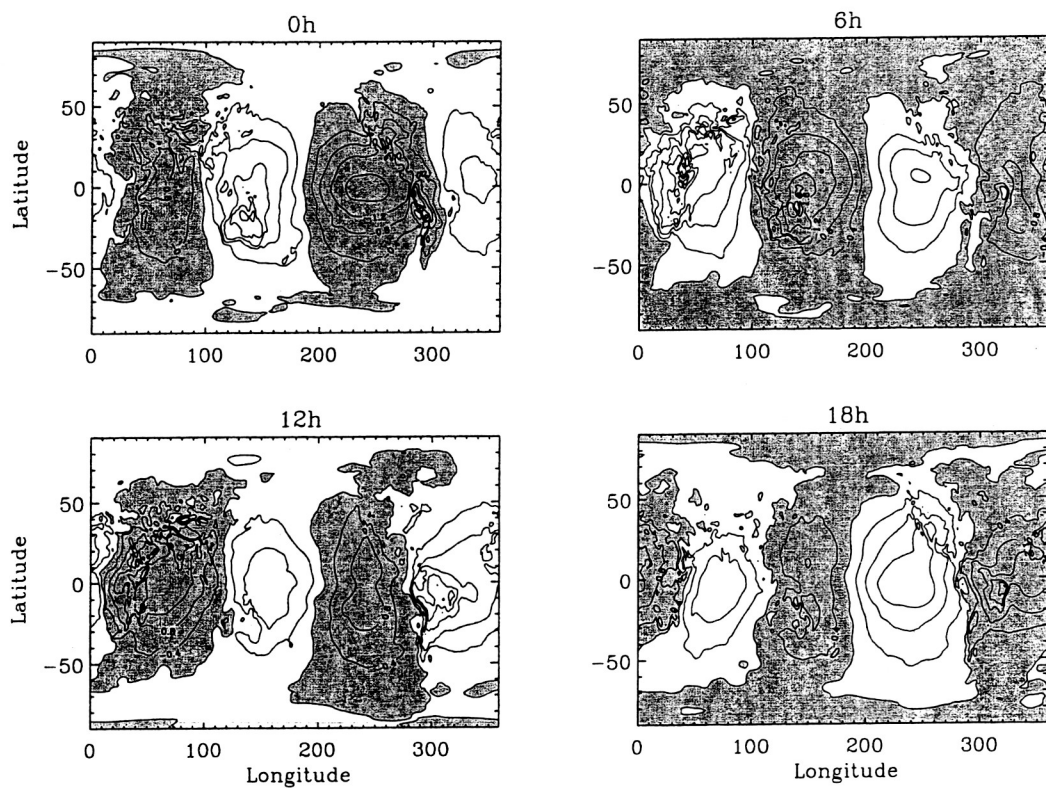


Fig. 1. Climatological daily cycle of surface pressure (mbar) calculated from 13 years of ECMWF analyses at 0000, 0600, 1200, and 1800 UT. Negative values are shaded. Contour interval is 0.4 mb.

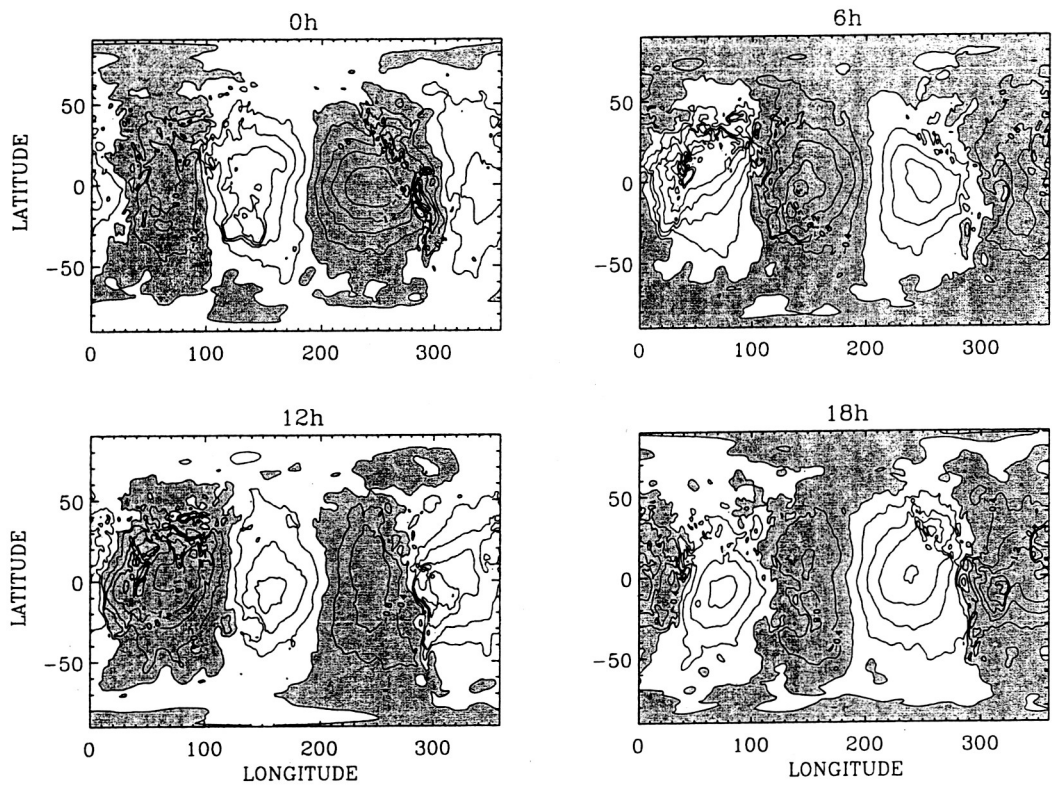


Fig. 2. As in Figure 1 but showing climatological daily cycle for March.

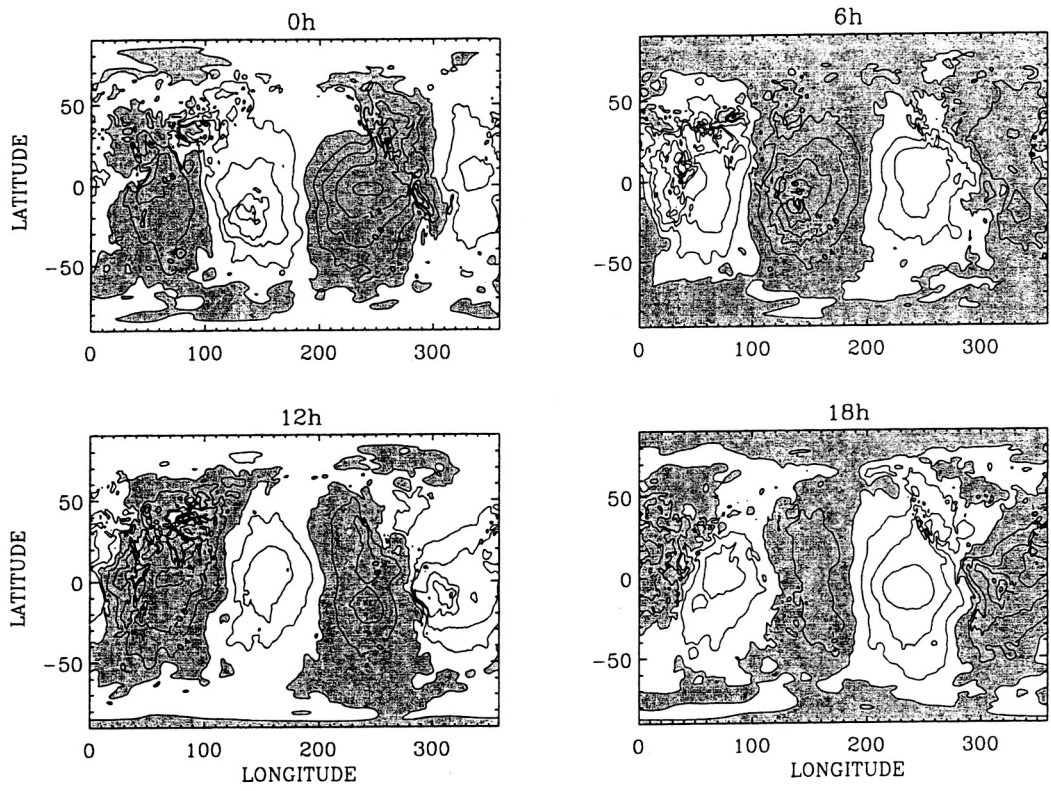


Fig. 3. As in Figure 1 but showing climatological daily cycle for June.

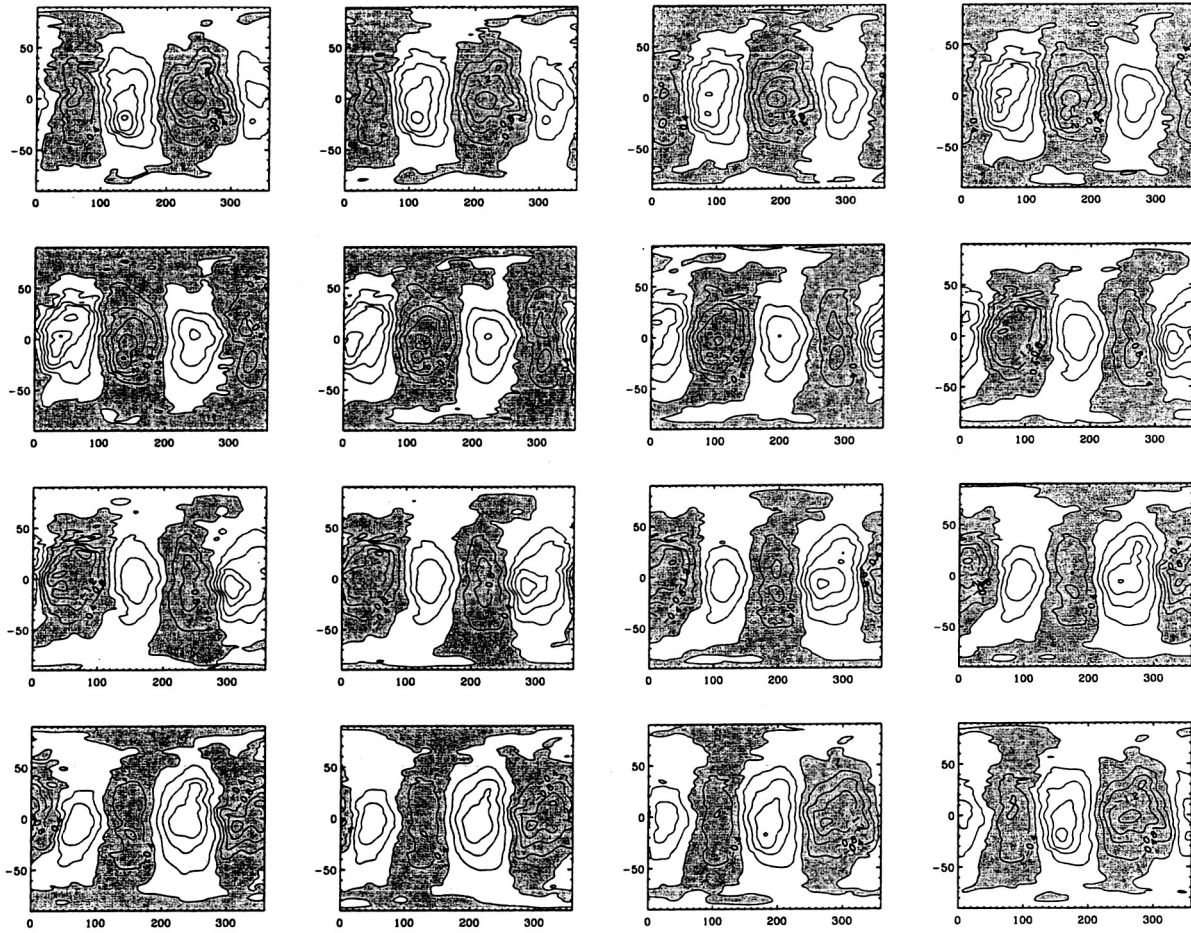


Fig. 4. Interpolated climatological daily cycle at 1.5 hour intervals. Time marches horizontally from the top left corner (0000 UT) to the bottom right corner (2230 UT).

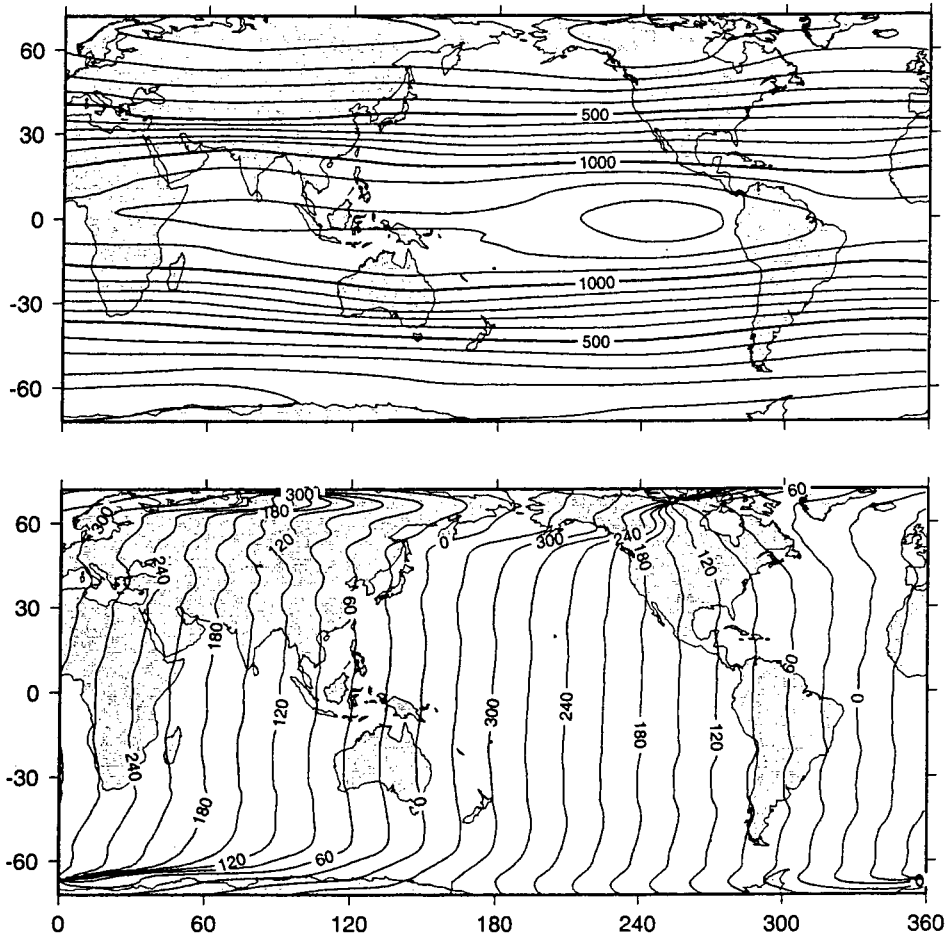


Fig. 5. Amplitude (μb) and Greenwich phase lags (degrees) of the $S_2(p)$ tide, calculated as described in the text. The phase contour interval of 30° corresponds to 1 hour in time.

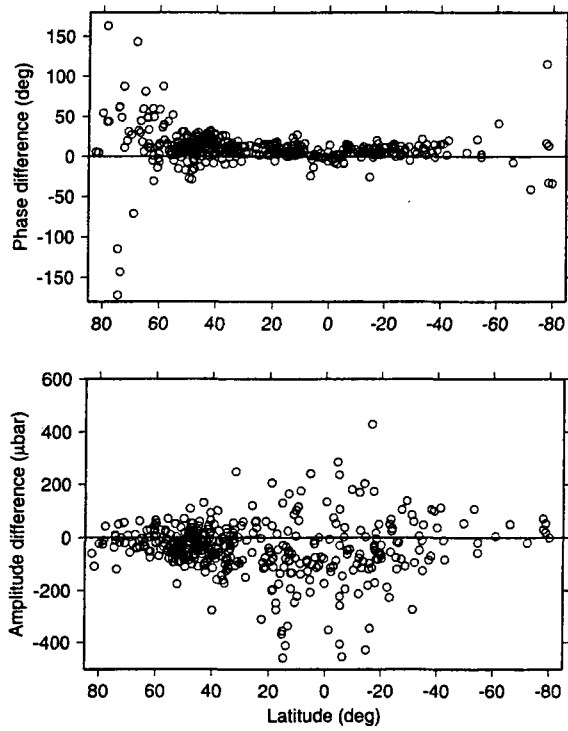


Fig. 6. Amplitude and phase differences between ECMWF-implied $S_2(p)$ tide and estimates based on 428 barometer stations. A small systematic error in the phases is readily apparent.

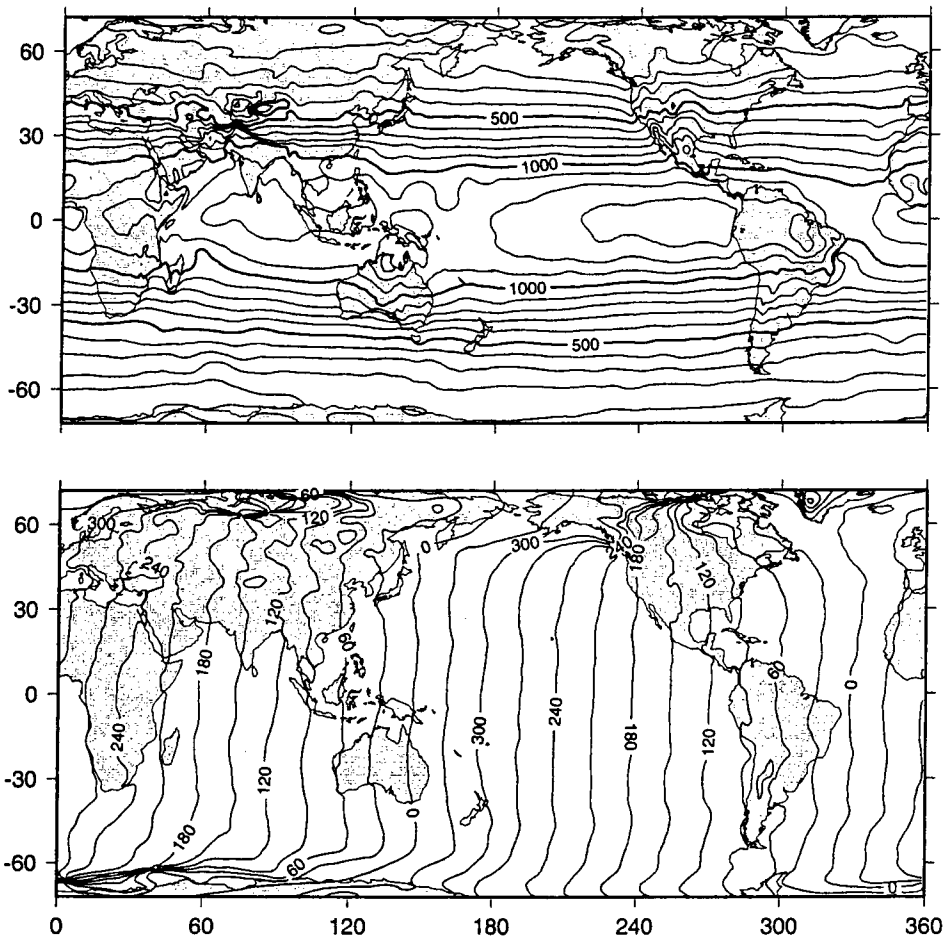


Fig. 7. Amplitude (μb) and Greenwich phase lags (degrees) of the $S_2(p)$ tide, as in Figure 5, except with the in-phase non-migrating component restored. This solution is denoted "ECMWF(2)" in Table 1.

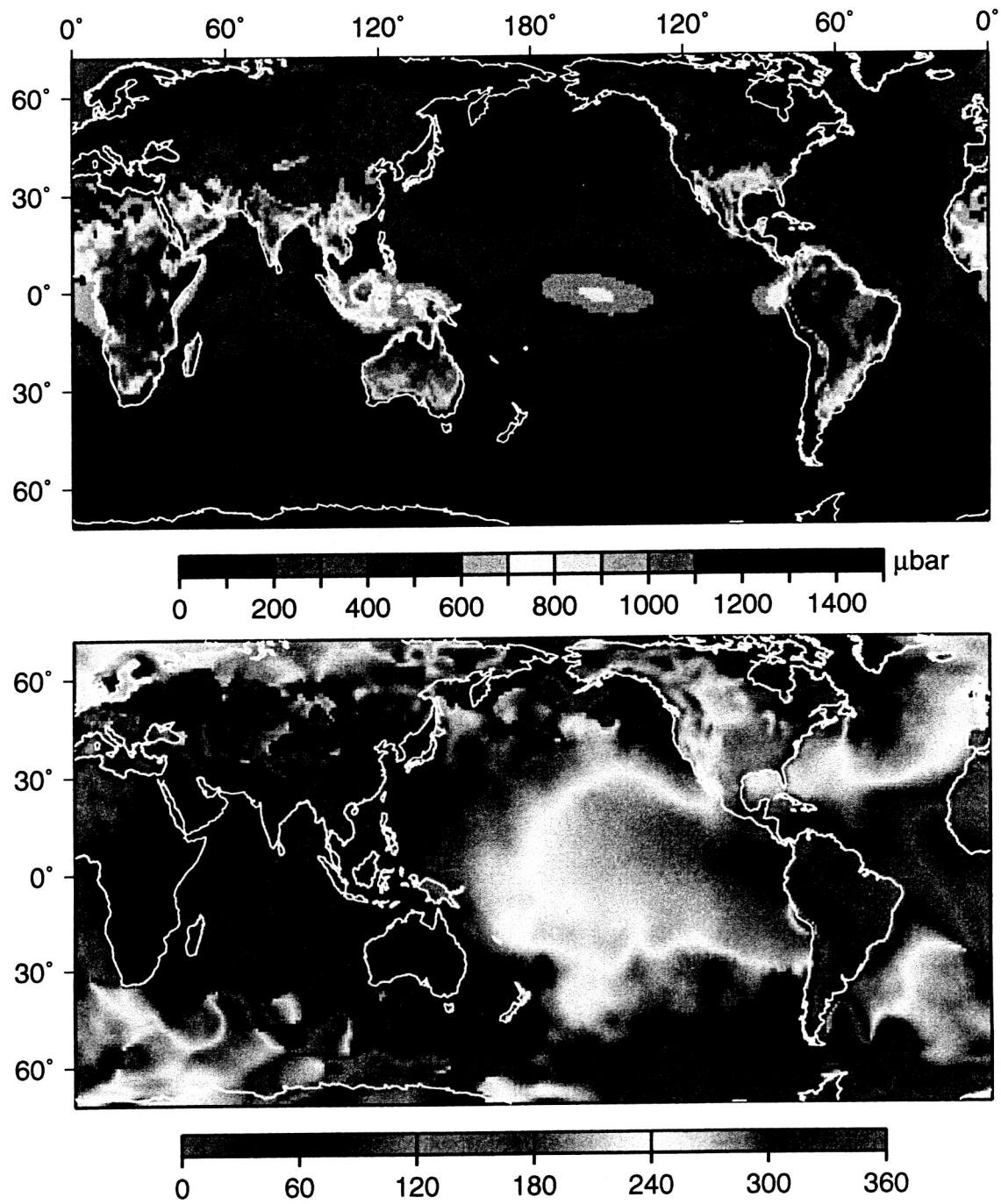


Fig. 8. Amplitude and Greenwich phase lags of the $S_1(p)$ tide, as deduced from ECMWF surface pressures.

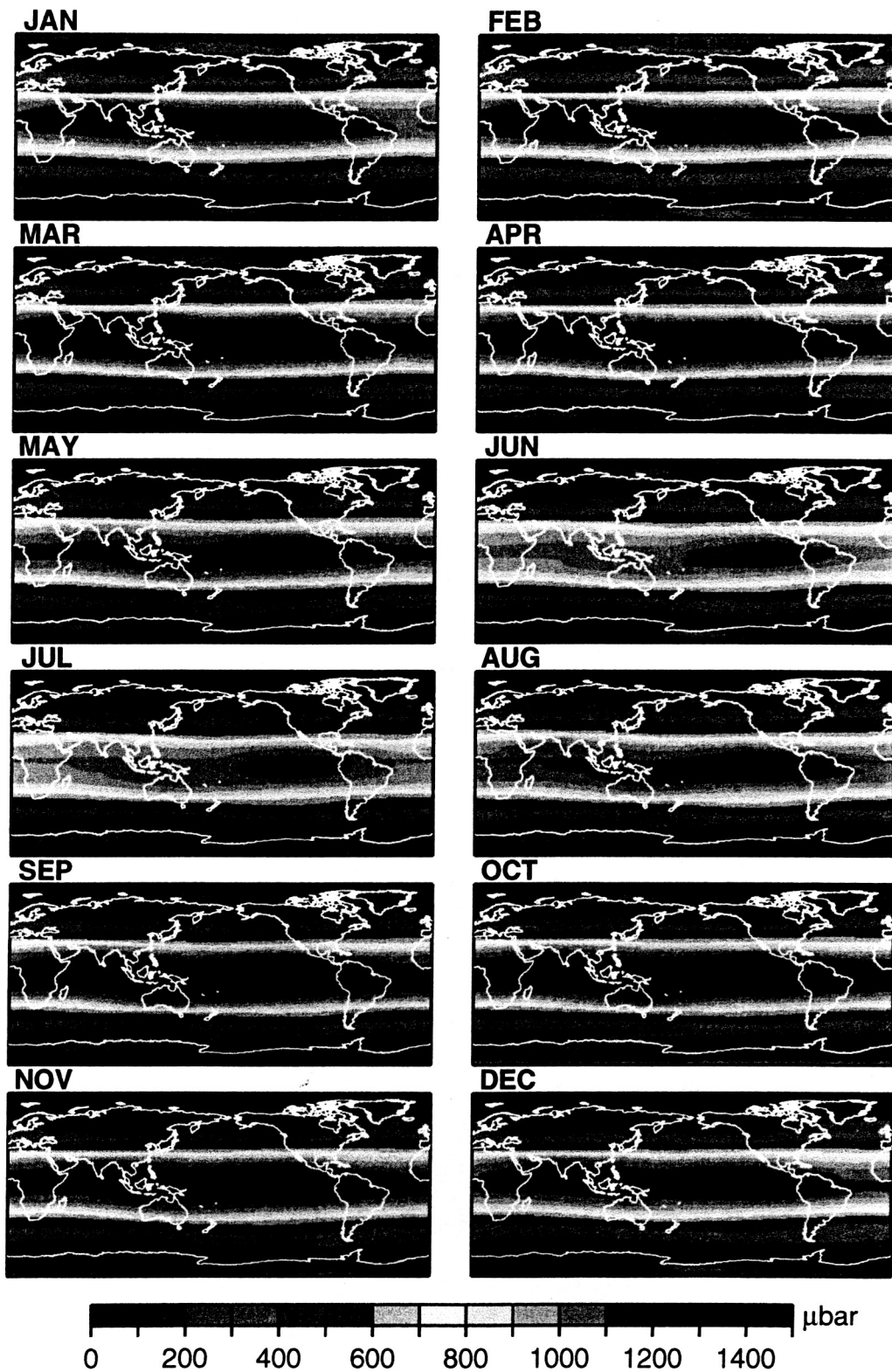


Fig. 9. Monthly mean amplitude of the $S_2(p)$ tide as deduced from ECMWF surface pressures.

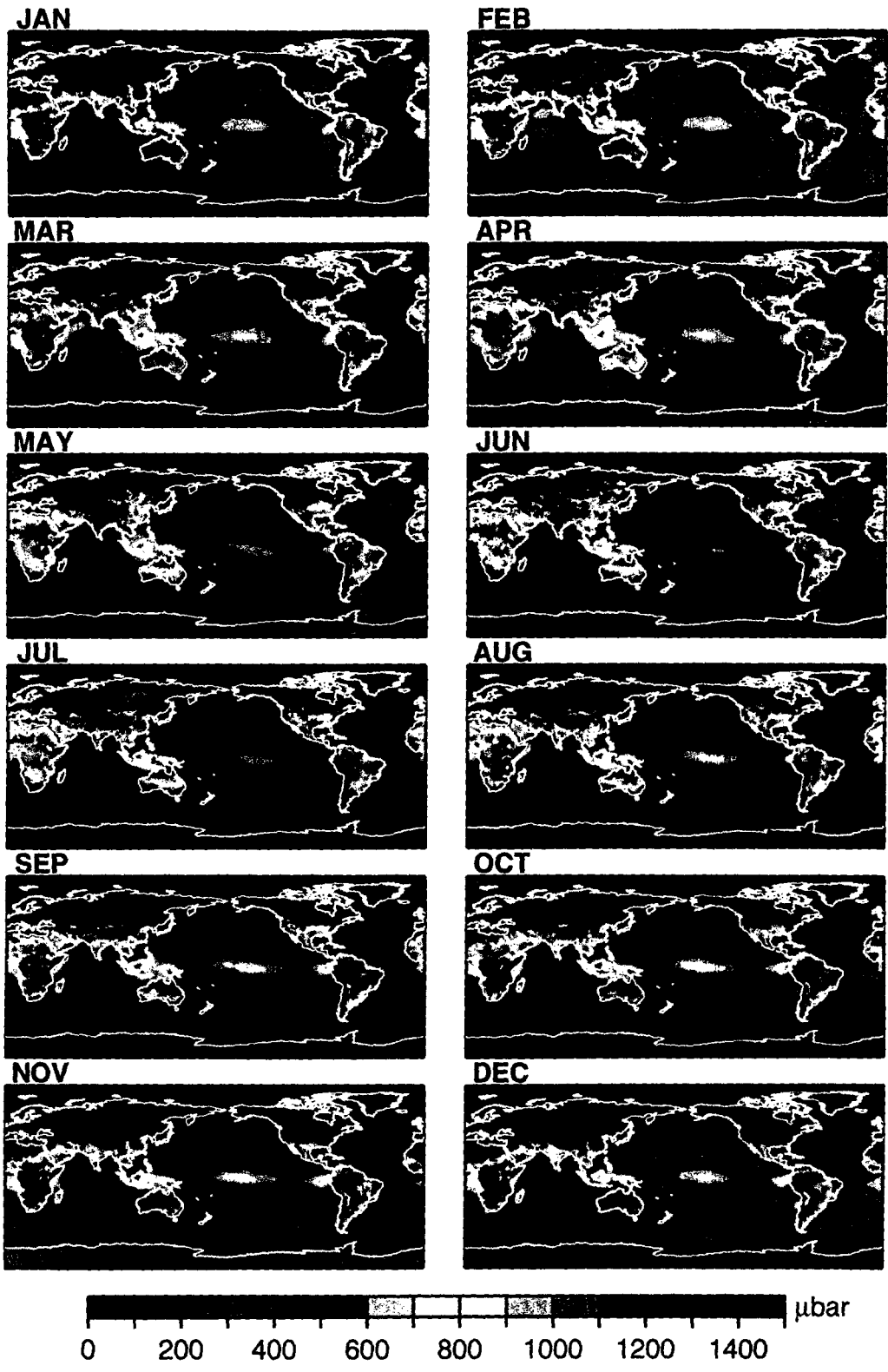


Fig. 10. Monthly mean amplitude of the $S_1(p)$ tide as deduced from ECMWF surface pressures.

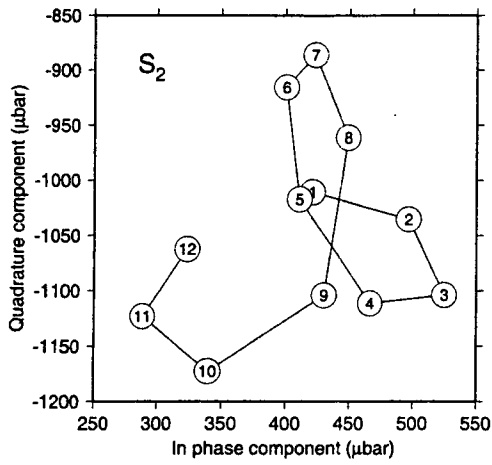


Fig. 11. Monthly estimates of the in-phase ($A_2 \cos \kappa_2$) and quadrature ($A_2 \sin \kappa_2$) components of the $S_2(p)$ tide, averaged over all tropical regions (latitudes $\leq 23^\circ$). Months are labeled 1–12.

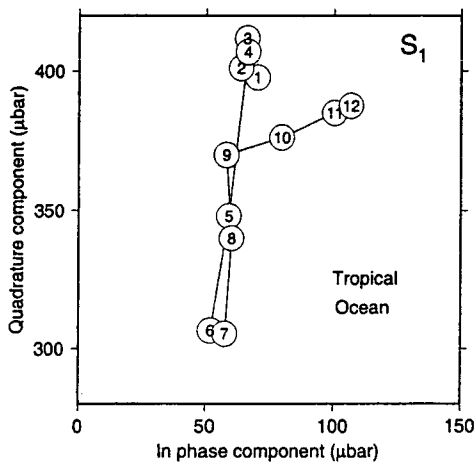
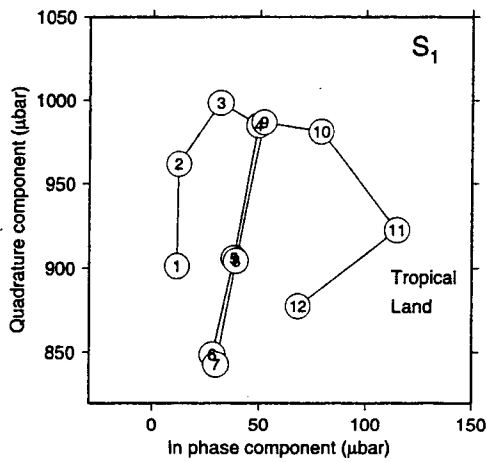


Fig. 12. As in Figure 11 but for $S_1(p)$, and separated into tropical ocean and land regions.

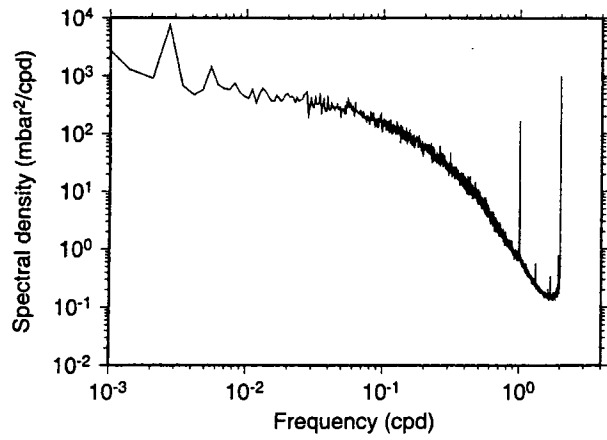


Fig. 13. Spectrum of the globally integrated ECMWF p_a series, based on the four-year span 1996-1999.

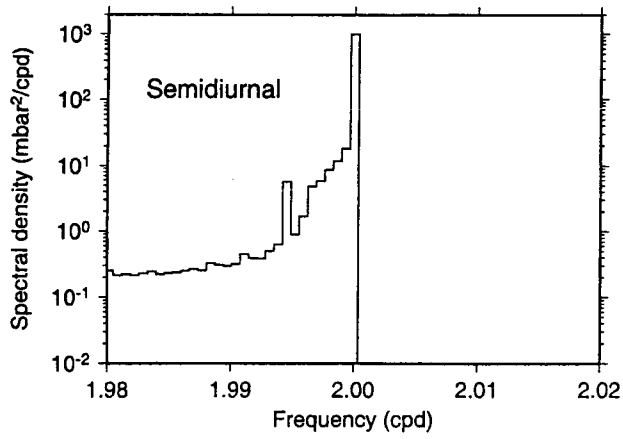
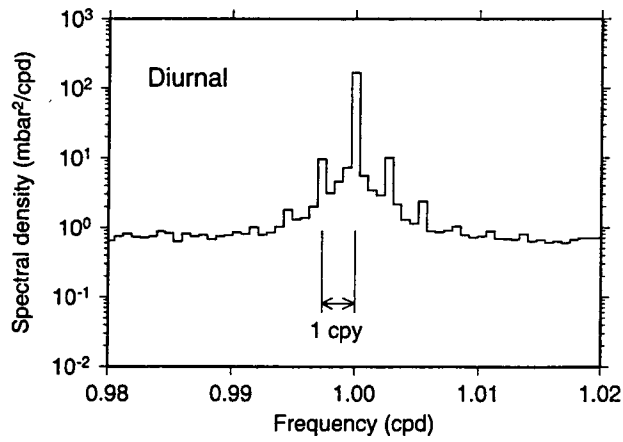


Fig. 14. Detailed views of the spectrum of Figure 13 surrounding the diurnal and semidiurnal peaks. Frequency resolution is 0.25 cpy.